Calculations of Propeller/Airframe Interference Effects Using the Potential/Multienergy Flow Method

T. Q. Dang*
Douglas Aircraft Company, Long Beach, California

This paper describes an analytical/computational model to predict propeller/airframe interference effects. In the present method, the propeller is modeled by an actuator disk and is assumed to have free-vortex blading. The flowfield consists of two potential flow regions of different stagnation conditions separated by a bound-vortex sheet located at the actuator disk and a free-vortex sheet located on the propeller slipstream. A newly developed technique of handling these vortex sheets is embedded into an existing finite-volume, full-potential code to analyze the flowfield. Comparisons of the results obtained using the present model to those from dissimilar models and some experimental data indicate that this simple method is adequate for integration studies of current ultra-high-bypass (UHB)-powered aircraft ranging from the subsonic takeoff/climbing flow regime to the transonic cruising condition.

I. Introduction

THE continuing quest to improve propulsive efficiency for aircraft operating in the subsonic and transonic flow regimes has caused growing interests in the ultra-high-bypass (UHB) or propfan engine as an alternative to the turbofan engine. Numerous studies[1,2] confirm that advanced, turboprop-powered aircraft offer substantial improvements in fuel consumption, up to 30% when compared to aircraft recently entering service and up to 50% when compared to the majority of aircraft in service. However, studies indicate that these dramatic gains can only be achieved if the propfan is properly integrated with the airframe so that undesirable propeller/airframe interference effects are minimized.[3,4] To quantify this interaction phenomenon, it is desirable to have a computational tool for the prediction of propeller effects on the flowfield around complex configurations.

The concern of an airplane designer is not focused on the details of the blade-to-blade flowfield but rather on the interference effects of the propeller on the airframe. In this case a simple, computationally easy and inexpensive, time-averaged method is preferable to a direct propeller analysis approach: the propeller is represented by an actuator disk[5] with proper jump conditions prescribed along the disk. This simplified model for simulating the presence of the propeller has been shown by several authors to be adequate for airframe integration studies.[6,7]

The flowfield behind propellers is inherently rotational due to the blade variable loading characteristics in the spanwise direction, flow incidence, and interference effects caused by the various airplane components. Consequently, an Euler formulation is required for the analysis of the flowfield within the propeller slipstream region behind the actuator disk. There are many recently developed methods to solve the Euler equations. Among these, the time-marching, finite-volume Euler schemes[8,9] solve for the primitive variables and have been applied to treat three-dimensional wing/body configurations. Yu et al.[6] and Whitfield and Jameson[7] have successfully employed these Euler algorithms to compute the flowfield around complex, three-dimensional propfan configurations.

If the configuration under consideration involves a propfan of the pusher type, such as the aft-pylon-mount pusher (see Fig. 1) selected by the Douglas Aircraft Company as the most attractive arrangement,[1] then previous calculations[10] indicate that the detailed structure of the rotational flowfield behind the propeller does not play an important role in propeller/airframe integration studies. In this case, the simpler potential/multienergy flow model[11,12] can be used to effectively simulate propeller/airframe interference effects. The flowfield is divided into two potential flow regions of different stagnation conditions separated by a bound-vortex sheet located at the actuator disk and a free-vortex sheet located on the propeller slipstream.

In the present study, the location and strength of the bound-vortex sheet are prescribed, but those of the free-vortex sheet must be calculated. A conceptually easy-to-understand procedure to handle discontinuities occurring at the free-vortex sheet is to use a full-potential approach with boundary-conforming grid at the propeller slipstream.[11,12] In this method, the grid surface leaving the actuator disk tip is either assumed to be the slipstream or modified during the calculation to conform to the actual slipstream. The latter is known as the adaptive grid technique. The equal-pressure condition across the free-vortex sheet, which implies a discontinuity in the velocity vector at this surface, can be satisfied by enforcing a double-valued potential on this surface.

Although this rather brute-force approach appears to be attractive, it has several restrictions and disadvantages. First, it is difficult to find and enforce the correct direction of the jump in the velocity vector across the free-vortex sheet. In practice, the jump in the velocity is taken to be along the streamwise grid lines. Second, the required use of the adaptive grid technique to satisfy the propeller slipstream kinematic condition is not desirable because it tends to slow down convergence and can introduce instabilities into the calculation, especially for complex geometries. Last, the implementation of the multigrid technique, a method of accelerating convergence, turns out to be complicated and cumbersome.

The findings of the studies summarized in Refs. 11 and 12 suggest the usefulness of a technique which can capture the free-vortex sheet during the calculation rather than fit a grid surface to it. In addition, these studies recognize that accurate modeling of this vortex sheet requires an effective way to satisfy the vorticity transport equation. The "smoothing" technique described in Ref. 13 is such a technique. It has been

Received Oct. 25, 1988; revision received June 14, 1989.

*Senior Engineer/Scientist, Aerodynamics Research and Technology; currently Assistant Professor, Dept. of Mechanical and Aerospace Engineering, Syracuse University, Syracuse, NY.

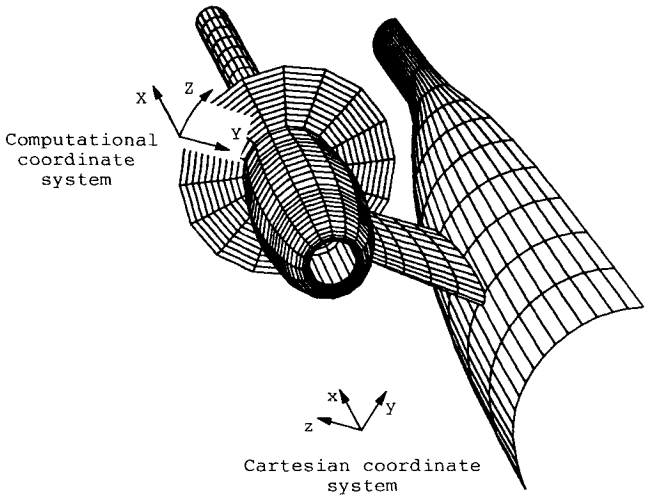

Fig. 1 Illustration of aft-fuselage/pylon/nacelle configuration with actuator disk.

developed to accurately treat all types of vortex sheets in transonic potential methods including trailing vortex sheets behind lifting surfaces. The idea is to remove singularities in the flowfield at the vortex sheets using generalized functions; all discontinuities are expressed in terms of the step function. The location and strength of the free-vortex sheet are determined by satisfying the no-flux boundary condition and the vorticity transport equation, respectively, and the remaining irrotational flowfield is determined from the continuity equation. The smoothing technique can be considered to be the external-flow version of the smoothing expansion technique,[14,15] which was developed earlier for periodic internal flows.

II. Potential/Multienergy Flow Actuator Disk Model

In this section, the model used to simulate flow through an aft-fuselage/pylon/nacelle-mounted, counter-rotating propfan of the pusher type is presented (see Fig. 1). As mentioned in the introduction, the presence of the propeller is replaced by a single actuator disk with proper jumps in the flow properties prescribed across it. In principle, the specifications of jumps in five flow properties are allowed in order to be consistent with the conservation laws of mass, momentum, and energy. These five independent quantities can be chosen to be the mass, the stagnation enthalpy, the entropy, the circumferential velocity (or swirl), and the radial velocity. Since the mass is conserved across the propfan, a maximum of only four jump quantities is required to be prescribed downstream of the actuator disk.

In the counter-rotating propfan, the forward propeller induces a swirl to the oncoming flow, and the aft propeller is designed to remove it. Hence, it is reasonable to assume that the jump in the swirl across the actuator disk is zero. As mentioned in the introduction, the propeller blades are taken to be of the free-vortex design so that the jump in the stagnation enthalpy across the propfan is constant. Finally, for simplicity, the flow is assumed to be isentropic across the actuator disk.

Consequently, the flowfield consists of two potential flow regions, each having different stagnation conditions, separated by a bound-vortex sheet at the actuator disk and a free-vortex sheet on the propeller slipstream (see Fig. 2). This is called the potential/multienergy flow actuator disk model. In this model, the location and strength of the bound-vortex sheet are prescribed; whereas those of the free-vortex sheet are not known a priori and must be determined during the calculation. Across this free-vortex sheet, two conditions must be satisfied:

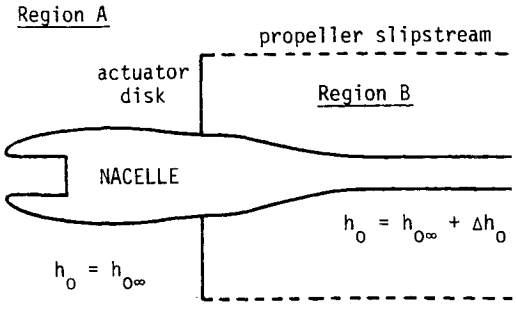

Fig. 2 Potential/multienergy flow actuator disk model for a counter-rotating propfan.

1) no-flux boundary condition: a kinematic condition which is satisfied by ensuring that the vortex sheet coincides with the stream surface emanating from the tip of the propeller and

2) equal pressure condition: a dynamic condition which can be satisfied by invoking the vorticity transport equation. As the two potential flow regions have different stagnation conditions, this condition implies that the velocity vector is discontinuous in magnitude and possibly in direction across the vortex sheet.

In practice, it is more useful to prescribe the propeller thrust loading coefficient rather than the jump in the stagnation enthalpy across the actuator disk. Using the one-dimensional, incompressible-flow Froude-Rankine analysis,[10,11] the jump in the stagnation enthalpy across the actuator disk is related to the thrust loading coefficient by

$$\Delta h_0 = \frac{1}{2}\left(\frac{T}{QA_d}\right) \tag{1}$$

where T is the thrust, Q is the dynamic pressure, and A_d is the propeller frontal area. Equation (1) is used to compute the required stagnation enthalpy jump corresponding to the prescribed thrust loading coefficient. Numerical simulations have shown that this relationship is accurate throughout the practical range of the thrust loading coefficient.[13]

Finally, the present method can be generalized to include jumps in the swirl and entropy across the actuator disk. In order to be consistent with the potential/multienergy flow model, these jumps must satisfy the following conditions:

$$\Delta(rV_\theta) = \text{const} \tag{2}$$

and

$$\Delta s = \text{const} \tag{3}$$

Equation (2) is the free-vortex flow condition and is derived from the Euler turbine equation.[16] Equation (3) ensures that the stagnation pressure jump across the actuator disk is constant so that the flowfield behind the actuator disk and within the propeller slipstream remains irrotational.

III. Theory

The smoothing technique described in Ref. 13 is used to handle discontinuities in the flowfield occurring at the bound- and free-vortex sheets. This technique consists of removing the singular part of the flowfield at these vortex sheets using generalized functions. Consider the velocity field. As the velocity vector is allowed to have jumps across the actuator disk and across the propeller slipstream, it can be expressed as

$$V = \nabla\phi + H(\sigma)\,H(\zeta)\,\Delta h_0 \nabla t \tag{4}$$

where $\sigma(x,y,z) = 0$ defines the prescribed actuator disk surface, $\zeta(x,y,z) = 0$ defines the propeller slipstream surface, and

H is the step function which is defined to be

$$H(\lambda) = 1 \quad \lambda > 0$$
$$= 0 \quad \lambda < 0 \tag{5}$$

In Eq. (4), the step functions are used to represent the jumps in the velocity vector across the bound- and free-vortex sheets. As a result, the remaining part of the velocity vector $\nabla\phi$ is smooth everywhere in the flowfield.

Taking the curl of Eq. (4), the vorticity vector is

$$\Omega = \delta(\sigma)\{H(\zeta)\Delta h_0[\nabla\sigma \times \nabla t]\} + \delta(\zeta)\{H(\sigma)\Delta h_0[\nabla\zeta \times \nabla t]\} \tag{6}$$

where the Dirac delta function[17] $\delta(\lambda)$ is defined to be zero everywhere except at $\lambda = 0$. As expected, the vorticity vector is zero everywhere except at the actuator disk, which is the first term on the right side of Eq. (6) and at the propeller slipstream, which is the last term on the right side of Eq. (6). In Eq. (4), the Clebsch[18] representation of the velocity vector is employed. This type of decomposition of the velocity vector into potential and rotational parts has been extensively employed in the calculations of three-dimensional rotational flows in turbomachines up to the subcritical flow regime using mostly analytical approaches.[14,15,19,20] Recently, a Euler-correction method was developed based on the Clebsch transformation of the Euler equation to model rotational flows in full-potential methods such as the vorticity field generated behind shocks[21] and the flowfield behind propellers of the forced-vortex blading.[10]

To determine the flowfield, the Clebsch variables are chosen to satisfy the equations of motion. For steady flow, the continuity equation is

$$\nabla \cdot (\rho V) = 0 \tag{7}$$

and the momentum equation, written in Lamb's form for isentropic flow, is

$$V \times \Omega = \nabla h_0 + F_B \tag{8}$$

where F_B is a body force per unit mass (local imposed acceleration) reacting on the fluid as a result of forces concentrated at the actuator disk. In the present model (see Fig. 2), given the locations of the actuator disk and the propeller slipstream, the stagnation enthalpy field is automatically known

$$h_0 = h_{0\infty} + H(\sigma)H(\zeta)\Delta h_0 \tag{9}$$

Furthermore, the body force F_B is concentrated at the actuator disk and can be expressed as

$$F_B = \delta(\sigma)H(\zeta)f_B \tag{10}$$

In the present approach, the potential part ϕ in Eq. (4) is determined using the continuity equation, and the Clebsch variable t is chosen to satisfy the momentum equation. On substituting Eqs. (6), (9), and (10) into the momentum equation, Eq. (8), along with the use of vector identities, several relationships are obtained. Along the actuator disk, the momentum equation relates the body force to the local flow conditions by

$$f_B = \{(<V>_d \cdot \nabla t - 1)\ \nabla\sigma - (<V>_d \cdot \nabla\sigma)\nabla t\}\ \Delta h_0 \tag{11}$$

where $<>_d$ denotes the average value in front of and behind the actuator disk. This body-force term is similar to the prescribed finite-volume force vector employed by Whitfield and Jameson[7] in their calculation of propeller/airframe interaction. Equation (11) can be used to derive Eq. (1) by linearizing the flowfield about the freestream condition.

Along the propeller slipstream behind the actuator disk, the momentum equation reduces to

$$(<V>_s \cdot \nabla t)\ \nabla\zeta - (<V>_s \cdot \nabla\zeta)\nabla t = \nabla\zeta \tag{12}$$

where $<>_s$ denotes the average value above and below the propeller slipstream. On imposing the no-flux boundary condition on the propeller slipstream, namely

$$<V>_s \cdot \nabla\zeta = 0 \tag{13}$$

the governing equation for the Clebsch variable t is obtained

$$<V>_s \cdot \nabla t = 1 \tag{14}$$

Conceptually, the Clebsch variable t is the classical Darwin-Lighthill-Hawthorne drift function.[22] The variation of t from streamline to streamline lying on the propeller slipstream surface is directly connected to the stretching and tipping of the vortex filaments located on this surface.

In principle, the entire flowfield can be computed by solving iteratively between the governing equations for the potential part, Eq. (7), and the governing equations for the rotational part, Eqs. (13) and (14), subjecting them to the appropriate boundary conditions. The following subsections describe methods of solving these equations along with the iterative procedure employed to determine the flowfield.

A. Solution Method for the Potential Function

When the smoothing technique is employed to remove singularities in the flowfield occurring at the bound- and free-vortex sheets, the gradient of ϕ is smooth across them. Consequently, ϕ is single-valued at these vortex sheets. Taking advantage of this fact, the potential part can be determined by solving the continuity equation using existing efficient and reliable full-potential flow solvers with minor modifications. In the present study, the Jameson/Caughey, finite-volume, full-potential method[23,24] is employed to determine the potential function ϕ. In this numerical scheme, the discretized quasilinear form of the potential equation utilized for formulating the iterative scheme is

$$L^n\{\phi^{n+1} - \phi^n\} = -\mathrm{Res}^n \tag{15}$$

where n is the iterative level, L is the potential equation operator, and Res is the residual of the continuity equation during the calculation. The discretized form of the residual is expressed in the computational space as

$$\mathrm{Res} \equiv \mu_{YZ}\delta_X(\rho hU + P) + \mu_{ZX}\delta_Y(\rho hV + Q)$$
$$+ \mu_{XY}\delta_Z(\rho hW + R) \tag{16}$$

In Eq. (16), μ is the averaging operator, δ is the differencing operator, h is the Jacobian of the transformation, (X,Y,Z) is the computational coordinate system (see Fig. 1), and (U,V,W) is the contravariant velocity vector. The artificial viscosity fluxes P,Q, and R are added in order to stabilize the algorithm in the supersonic flow regions.

When the present power method is included, the general form of the operator L and the artificial viscosity fluxes remain unchanged. The only modifications involved are in the evaluation of the cell-averaged velocity, speed of sound, and density, which appear in the expression for the residual of the continuity equation and in the coefficients of the potential equation operator.

As an illustration of the method of computing cell-averaged quantities, consider the velocity vector. According to Eq. (4), the velocity vector takes on appropriate forms depending on the location of the cell under consideration (see Fig. 3). In the present study, the grids are constructed to conform to the

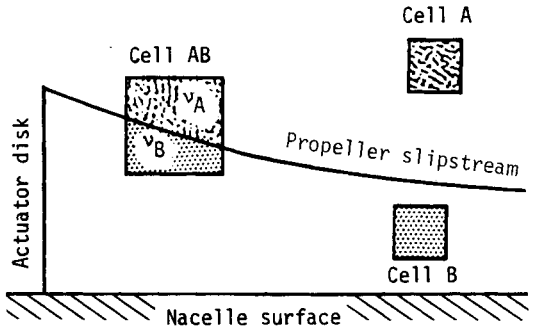

Fig. 3 Method of weighted-averaged volume applied to cell-averaged quantities.

specified actuator disk location and size but not to the propeller slipstream location since it is not known a priori. Hence, in general, there exist cells which lie in both regions A and B, such as cell AB shown in Fig. 3. In this case, the method of volume weight-averaged is used to evaluate the cell-averaged quantities. For cell A, which lies in region A, the cell-averaged velocity is computed from

$$V = \nabla\phi \tag{17}$$

For cell B, which lies in region B, the cell-averaged velocity is computed from

$$V = \nabla\phi + \Delta h_0 \nabla t \tag{18}$$

and finally, for cell AB, which lies in both regions, the cell-averaged velocity is computed from

$$V = \frac{\nu_A}{\nu_A + \nu_B}\nabla\phi + \frac{\nu_B}{\nu_A + \nu_B}(\nabla\phi + \Delta h_0 \nabla t) \tag{19}$$

where ν_A and ν_B are the partial volumes of cell AB which lie in regions A and B, respectively (see Fig. 3).

B. Solution Method for the Propeller Slipstream Location

The propeller slipstream along with the actuator disk form boundaries which separate regions A and B (see Fig. 2). In the present method, the location of the actuator disk surface is given; whereas the propeller slipstream geometry must be determined. The propeller slipstream kinematic condition, Eq. (13), is used to compute the location of the propeller slipstream surface. As the computational coordinate system employed in the original full-potential solver is cylindrical-like[24] (see Fig. 1), it is convenient to define the propeller slipstream surface in the computational space

$$\zeta \equiv Y - F(X,Z) \tag{20}$$

On using this definition, Eq. (13) written in the computational space is

$$<U>_s \frac{\partial F}{\partial X} + <W>_s \frac{\partial F}{\partial Z} = <V>_s \tag{21}$$

Given the solution of the velocity field from the previous iteration, Eq. (21) reduces to a linear, first-order, partial-differential equation of the hyperbolic type. In order to solve it, boundary conditions for F need to be prescribed at the actuator disk. The initial location of the propeller slipstream surface is at the actuator disk tip. Finally, Eq. (21) is solved numerically using the implicit, second-order accurate Crank-Nicholson scheme.

Two types of power-simulation modes have been developed to investigate the importance of the propeller slipstream geometry. In the assumed propeller slipstream mode, the propeller slipstream is taken to be the grid surface emanating from the tip of the actuator disk, and this grid surface is kept fixed during the calculation. In the captured slipstream mode, the initial guess of the propeller slipstream is chosen to be this grid surface, but the propeller slipstream geometry is constantly updated during the calculation through Eq. (21). The outcome of this investigation is given in Sec. IV.

C. Solution Method for the Drift Function

In the present formulation, the drift function t is employed to describe the convection of the vortex rings lying on the propeller slipstream surface. Hence, it is necessary to compute the drift function on the propeller slipstream surface only. The governing equation for t, Eq. (14), written in the computational space is

$$<U>_s \frac{\partial t}{\partial X} + <V>_s \frac{\partial t}{\partial Y} + <W>_s \frac{\partial t}{\partial Z} = 1 \tag{22}$$

Equation (22) can be simplified by invoking the propeller slipstream kinematic condition. On the propeller slipstream surface, in addition to Eq. (13), the no-flux boundary condition also requires the jump in the velocity vector across this surface be tangent to it. On using Eq. (4), this condition translates to

$$\nabla t \cdot \nabla \zeta = 0 \tag{23}$$

Equation (23) imposes a constraint on the derivatives of t. In the computational space, the expression becomes

$$\frac{\partial t}{\partial Y} = I \frac{\partial t}{\partial X} + K \frac{\partial t}{\partial Z} \tag{24}$$

where $I = I(x,y,z,F)$ and $K = (x,y,z,F)$ are defined in Ref. 25. On using this relationship, Eq. (22) reduces to

$$(<U>_s + I <V>_s)\frac{\partial t}{\partial X} + (<W>_s + K <V>_s)\frac{\partial t}{\partial Z} = 1 \tag{25}$$

Similar to the governing equation of the propeller slipstream location, Eq. (25) is of the hyperbolic type. In order to solve this equation, initial values for t need to be prescribed. From the zero-jump conditions in the radial and circumferential velocities across the actuator disk, the initial values for t along the tip of the actuator disk are taken to be zero. As before, the implicit, second-order, accurate, Crank-Nicholson scheme is used to solve Eq. (25).

D. Iterative Procedure

The flowfield is determined by solving iteratively between the potential and the rotational parts in Eq. (4). The following iterative procedure is employed.

1) Set the initial velocity field to the freestream condition.

2) Update the potential function ϕ using a modified version of a finite-volume, full-potential method described in subsection IIIA. In this step, the implementation of the volume weight-averaged procedure to compute cell-averaged quantities results in an increase of 25% in the computing time per multigrid cycle over the original full-potential flow solver.

3) Update the drift function t by solving Eq. (25). The computing time required in this step is negligible compared to the second step since the calculation is performed only on the propeller slipstream surface behind the actuator disk.

4) If the assumed slipstream mode is employed, bypass this step. Otherwise, in the captured slipstream mode, the propeller slipstream ζ is updated by solving Eq. (21) from the actuator disk to the downstream boundary. Again, the computing

time required in this step is negligible compared to the second step.

5) Check for convergence and repeat steps 2–5 until convergence is attained.

Numerical experiments show that the computing time per multigrid cycle is roughly 30% more than that of the original code. When the assumed slipstream mode is employed, the number of multigrid cycles required to obtain a converged solution comparable to the prop-off case remains the same, independent of the magnitude of the thrust loading coefficient. However, more iterations are required when the captured slipstream mode is employed. Specifically, in the transonic flow regime where the thrust loading coefficient is small, the number of multigrid cycles required to obtain a converged solution comparable to the propoff case remains unchanged. In the subsonic flow regime where the thrust loading coefficient is large, the required number of multigrid cycles is increased by about 50%. Finally, this proposed iterative procedure is stable throughout the practical range of the thrust loading coefficient.

IV. Results

The present method for simulating propeller effects has been implemented into an existing multigrid, finite-volume, full-potential code.[24] This code was originally developed to analyze the transonic flowfield about aft-fuselage/pylon/nacelle configurations without propeller effects. Generation of the computational grid for this complex configuration was accomplished using the hybrid conformal-mapping/algebraic technique of Halsey.[26] This method conforms grid lines to the specified actuator disk shape.

Figure 4 illustrates comparisons of the pressure distributions on the pylon, nacelle, and fuselage stations between the prop-off and prop-on cases for the configuration A in the subsonic flow regime. In this configuration, the actuator disk is located at a nondimensionalized axial distance of 2. These results show that the effect of power is prominent in the low-speed regime: the pressure level is modified over the entire aft portion of the airplane. As expected, the presence of the propfan results in a higher flow velocity in front of the propeller as shown by the negative higher *Cp* level of the prop-on curves for $x < 2$. Along the nacelle station, the presence of the propfan produces a jump in the static pressure across it. Along the fuselage station, power effects introduce an adverse pressure gradient near the actuator disk plane indicating a potential flow separation region. It is important to note that the same conclusion cannot be drawn for the nacelle station because the stagnation quantities in front of and behind the actuator disk are different. In fact, for this nearly incompressible flow case, the velocity plot on the nacelle surface shows that the velocity increases smoothly across the actuator disk and reaches a downstream value higher than the freestream value.[13]

Figure 5 shows comparisons similar to Fig. 4, but at the transonic cruising condition. This figure indicates that power effects are less prominent in the transonic flow regime with a narrower domain of influence. When shocks appear on the pylon near the propfan, the effects of power are to increase the shock strength and move it further downstream resulting in higher wave drag and earlier onset of shock-induced flow separation. Note that the potential separated flow region on the fuselage station, which is triggered by the presence of the propfan in the subsonic flow regime, does not appear to exist in the transonic flow regime.

Figures 6 and 7 demonstrate the importance of using the correct propeller slipstream geometry in predicting propeller/airframe interference effects. These calculations are performed in the subsonic flow regime where the effect of power is prominent. In addition, a lifting case is chosen to test the robustness of the method in capturing propeller slipstream geometries, which are highly nonconformed to the employed grid distribution. Figure 6 illustrates the propeller slipstream geometries at the symmetry employed in the assumed slipstream mode and calculated by the captured slipstream mode. As expected, the captured propeller slipstream geometry shows a contraction effect and becomes aligned with the freestream flow direction in the downstream region. Figure 7 shows comparisons of the *Cp* increment due to power on the pylon and nacelle stations between the results obtained using the assumed and captured slipstream modes. Here, the *Cp* increment is defined to be the difference in *Cp* between the prop-on and prop-off solutions. This figure shows that the

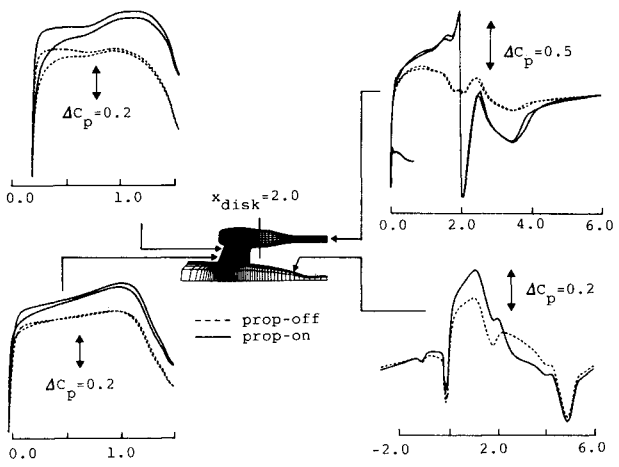

Fig. 4 Comparison of surface pressure distributions for configuration A at $M_\infty = 0.2$, $\alpha = -3$ deg, and $T/QA_d = 2$.

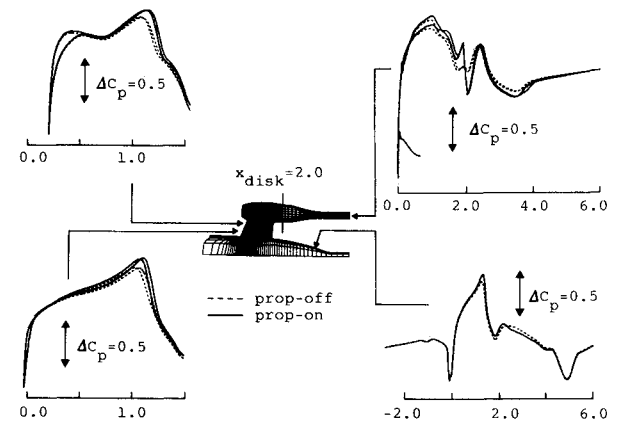

Fig. 5 Comparison of surface pressure distributions for configuration A at $M_\infty = 0.76$, $\alpha = -3$ deg, $T/QA_d = 0.16$.

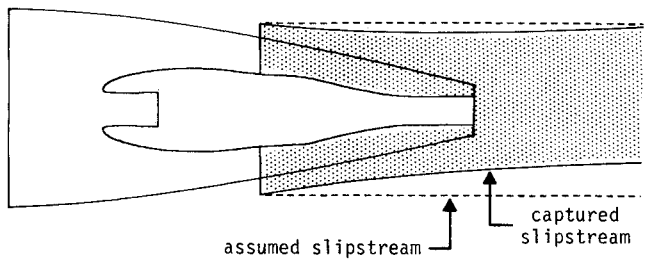

Fig. 6 Comparison of assumed and captured slipstream geometries at the nacelle symmetry plane for configuration B at $M_\infty = 0.2$, $\alpha = 5$ deg, and $T/QA_d = 2$.

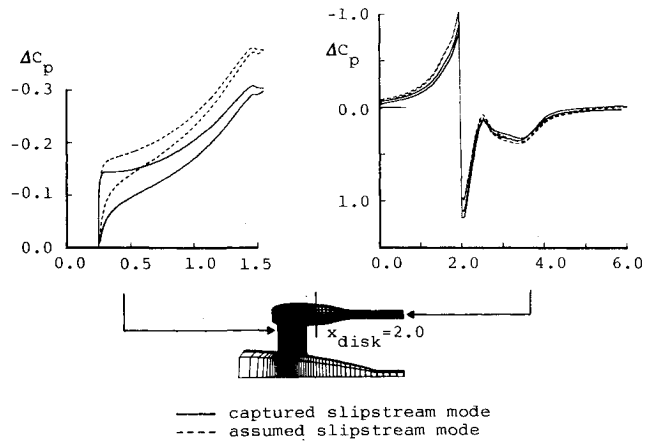

Fig. 7 Effect of slipstream geometries on *Cp* increment due to power for configuration B at $M_\infty = 0.2$, $\alpha = 5$ deg, and $T/QA_d = 2$.

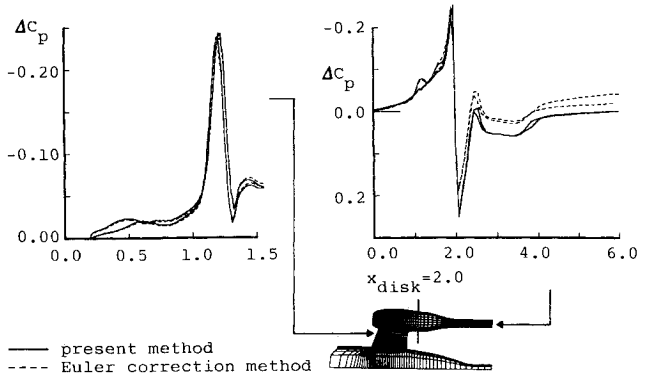

Fig. 8 Comparison of *Cp* increment due to power between the present method and the Euler-correction method for configuration A at the transonic cruising condition.

solutions obtained using the assumed slipstream geometry overpredict the *Cp* increment by as much as 25% on the pylon station. The same observation can be made for the portion of the nacelle station that does not include the region occupied by the actual propeller blades. This large overprediction is due to the fact that the flow enters the higher energy region not only through the actuator disk surface, but also across the employed assumed-propeller-slipstream geometry, which is larger than the actual shape (see Fig. 6). In the transonic flow regime where the thrust loading coefficient is small, numerical experiments indicate that the sensitivity of the solutions on the propeller slipstream geometry is small, except for flow conditions and configurations which produce strong shocks near the pylon trailing edge.

To validate the method, a comparison of its predictions with experimental data is necessary. Unfortunately no high-speed test data is available. However, there exists a Euler-correction method[10] to verify with the present method. The Euler-correction method was developed earlier for propeller/airframe integration studies in the transonic flow regime where the thrust loading coefficient is small. In the Euler-correction method, the propfan is also modeled by an actuator disk, but the propeller is assumed to be of the forced-vortex blading type—namely the stagnation enthalpy jump is allowed to vary in the blade spanwise direction. In the following calculations performed with the Euler-correction method, the employed propeller loading characteristics is of the tip-loaded blading and is typical of many advanced propeller blades.[10]

Figure 8 shows comparisons of the predicted *Cp* increment due to power between the solutions obtained using the present method and the Euler-correction method for configuration A at the transonic cruising condition. Along the pylon station, the two solutions are virtually identical. Both methods give the same predictions of the shock movement and shock strength as can be seen by the spike in the *Cp* increment curve near the pylon trailing edge. Along the nacelle station, the comparison deteriorates behind the actuator disk because the Euler-correction method employs small perturbation approximations for the rotational flow region behind the actuator disk.

In the subsonic flow regime, test data are available for code validation, but for a different configuration. While the calculation method is limited to a pylon/nacelle mounted on a body infinite in the upstream direction, test results are available for two configurations at $M_\infty = 0.2$ and $T/QA_d = 2$: a wing-fuselage pylon/nacelle with and without a tail. The experimental data for the configuration with a tail do agree with the calculations for the prop-off condition using a corrected value for the freestream angle of attack. Accordingly, the prop-off/on test data for the configuration with a tail are used to validate the *Cp* increments due to power predicted by the present method. In addition, solutions obtained using the panel

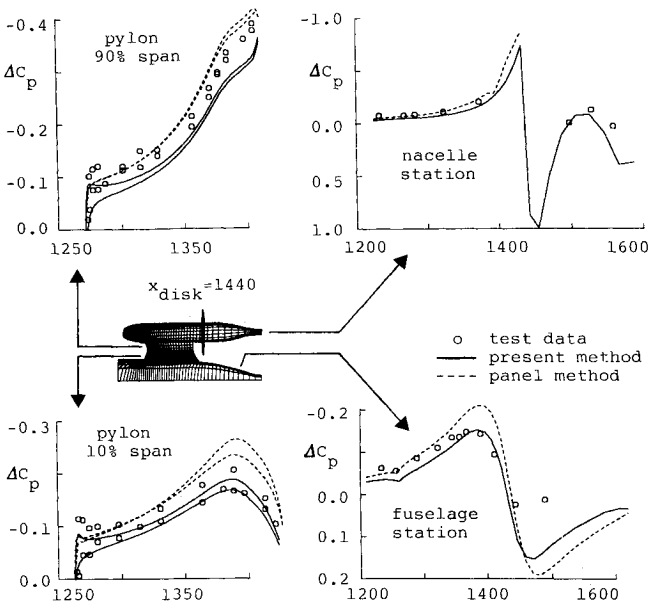

Fig. 9 Comparison of test data and predicted *Cp* increment due to power for configuration *C* at $M_\infty = 0.2$, $\alpha = -3$ deg, and $T/QA_d = 2$.

method[27] are also used for comparison with those calculated by the present method. In the panel method, the mutual aerodynamic interference effects between the propeller and the airframe are approximated by superimposing the time-averaged, isolated propeller on to a "standard" panel solution for the remaining part of the aircraft. This panel method and the method described in this paper employ very different models and approximations to simulate propeller/airframe interference effects.

Figure 9 summarizes the low-speed, code-validation study through comparisons of the *Cp* increments due to power on the pylon, fuselage, and nacelle stations. This figure indicates that the agreements in the overall trend between the test data and the computational results are very good. Along the fuselage station, Fig. 9 shows good agreement between test data and computational results for the axial locations in front of the actuator disk plane which is located at $x_{\text{disk}} = 1440$, but poor agreement is found for the axial locations behind it. Referring to Fig. 4, which illustrates the adverse pressure gradient introduced into the fuselage station in the presence of the propfan, Fig. 9 appears to confirm the existence of a flow separation region on the fuselage portion located behind the actuator disk plane. The discussion on the importance of the

fuselage boundary layer is reported in Ref. 24 and is outside the scope of the present paper. Finally, a close look at these results indicates that the present method consistently underpredicts the *Cp* increment level at all stations. These observations suggest that either the estimated thrust loading coefficient of the experiment is slightly off or the "calibration"[25] of the thrust loading coefficient in the present method needs to be improved. Another possibility could be associated with the isentropic flow assumption employed in the present calculations. For nonisentropic flow across the actuator disk, a higher increase in the stagnation enthalpy is required for the same thrust-loading coefficient, hence a larger *Cp* increment level will be generated. The modeling of the overall propeller efficiency can easily be incorporated into the present method by including an additional rotational term in Eq. (4) to account for the entropy increase across the actuator disk.[21]

V. Conclusions

This paper presents a useful technique to simulate propeller/airframe interference effects for aircraft operating up to the transonic flow regime. The configuration under consideration is an aft-fuselage/pylon/nacelle-mounted, counter-rotating propeller of the pusher type. The propeller is modeled by an actuator disk across which the prescribed jump in the stagnation enthalpy is assumed to be constant. Consequently, the flowfield consists of two potential flow regions of different stagnation conditions separated by a bound-vortex sheet located at the actuator disk and a free-vortex sheet located on the propeller slipstream.

In the present study, the location and strength of the bound-vortex sheet are prescribed; whereas those of the free-vortex sheet must be calculated. The smoothing technique is used to analyze the flowfield: singularities occurring at the vortex sheets are removed through the use of the step function. The location and strength of the free-vortex sheet are determined by satisfying the no-flux boundary condition and the vorticity transport equation, respectively, and the remaining irrotational flowfield is determined from the continuity equation using a modified version of an existing finite-volume, full-potential flow solver.

Numerical experiments indicate that the proposed method is robust and efficient throughout the practial range of the thrust-loading coefficient encountered in the subsonic and transonic flow regimes. This method is a big improvement over the Euler-correction method,[10] which, in theory, does not apply in the practical subsonic flow regime where the thrust loading coefficient is large. It is also an improvement over the panel method[27] because the panel method cannot handle transonic flows. The main advantage of the present method over those based on the Euler schemes[6,7] is its ease of implementation into existing state-of-the-art, well-proven, efficient, full-potential methods, which are presently the primary transonic flow computational tools used in the commercial transport aircraft industry. Finally, comparisons of the results obtained using the present model and the limited amount of available test data indicate that this simple model can be used to effectively simulate propeller effects about aft-fuselage/pylon/nacelle-mounted, counter-rotating propellers of the pusher type.

Acknowledgments

The work reported in this paper was conducted under the sponsorship of the Independent Research and Development Program of the McDonnell Douglas Corporation. The author would like to acknowledge N.D. Halsey and A. Shmilovich for their assistance in the grid generation method and the unpowered version of the potential flow solver, respectively.

References

[1]Page, M. A., Ivey, D. M., and Welge, H. R., "Ultra High Bypass Engine Applications to Commercial and Military Aircraft," SAE Paper 86-1720, Oct. 1986.

[2]Van't Riet, R., Lewerenz, W. T., and Donelson, J. E., "UHB Technology Flight Validation Program," Douglas Paper 7702, June 1986.

[3]Welge, H. R., Neuhart, D. H., and Dahlin, J. A., "Analysis of Mach 0.8 Turboprop Slipstream Wing/Nacelle Interactions," Douglas Aircraft Co., Long Beach, CA, NASA CR-166214, July 1981.

[4]Smith, R. C., and Levin, A. D., "Prop-Fan Installation Aerodynamics of a Supercritical Swept Wing Transport Configuration," AIAA Paper 81-1563, July 1981.

[5]Horlock, J. H., *Actuator Disk Theory*, McGraw-Hill, New York, 1978.

[6]Yu, N. J., Samart, S. S., and Rubbert, P. E., "Flow Prediction for Propfan Configurations using Euler Equations," AIAA Paper 84-1645, 1984.

[7]Whitfield, D. L., and Jameson, A., "Three-Dimensional Euler Equation Simulation of Propeller-Wing Interaction in Transonic Flow," AIAA Paper 83-0236, 1983.

[8]Jameson, A., Schmidt, W., and Turkel, E., "Numerical Solutions of the Euler Equation by Finite Volume Methods Using Runge-Kutta Time-Stepping Schemes," AIAA Paper 81-1259, June 1981.

[9]Jameson, A., and Baker, T. J., "Multigrid Solution of the Euler Equations for Aircraft Configurations," AIAA Paper 84-0093, Jan. 1984.

[10]Dang, T. Q., "Simulations of Propeller/Airframe Interference Effects Using an Euler Correction Method," *Journal of Aircraft*, Vol. 26, No. 11, Nov. 1989, pp. 994-1001.

[11]Zaretsky, B., Dang. T. Q., Shmilovich, A., and Halsey, N. D., "Calculation of Propeller Effects on Axisymmetric Nacelles With and Without Inlets," Douglas Aircraft Co., Long Beach, CA, Rept. MDC J4920, Oct. 1986.

[12]Zaretsky, B., and Shmilovich, A., "Calculation of Propeller Effects for Isolated Three-Dimensional Inlets," Douglas Aircraft Co., Long Beach, CA, Memo C1-E82-A&A-87-1344, Oct. 1987.

[13]Dang, T. Q., "Accurate Treatment of Vortex Sheets for the Transonic Potential Equation with Application to Propeller Slipstream," Douglas Aircraft Co., Long Beach, CA, Rept. MDC K1342, June 1988.

[14]McCune, J. E., and Dang, T. Q., "Periodic Internal Flows," *Proceedings of the ASME Conference on Computations of Internal Flows: Methods and Applications*, edited by P. M. Sockel and K. N. Ghia, 1984, pp. 123-128.

[15]Dang, T. Q., "A Three-Dimensional Blade Design Method to Control Secondary Flow," Ph.D. Thesis, Department of Aeronautics and Astronautics, Massachusetts Institute of Technology, Cambridge, June 1985.

[16]Oates, G. C., *Aerothermodynamics of Gas Turbine and Rocket Propulsion*, AIAA Education Series, New York, 1984.

[17]Lighthill, M. J., *An Introduction to Fourier Analysis and Generalized Functions*, Cambridge Univ., 1969.

[18]Lamb, H., *Hydrodynamics*, Dover, 1960.

[19]McCune, J. E., and Hawthorne, W. R., "The Effects of Trailing Vorticity on the Flow Through Highly-Loaded Cascades," *Journal of Fluid Mechanics*, Vol. 74, 1976, pp. 721-740.

[20]Hawthorne, W. R., McCune, J. E., Mitchell, N. A., Tan, C. S., "Nonaxisymmetric Flow Through an Annular Actuator Disk: Inlet Distortion Problem," *ASME Journal of Enginering for Power*, Vol. 100, 1978.

[21]Dang, T. Q., and Chen, L. T., "An Euler Correction Method for Two- and Three-Dimensional Transonic Flows," AIAA Paper 87-0522, Jan. 1987, also *AIAA Journal* (to be published).

[22]Hawthorne, W. R., "Engineering Aspects," *Research Frontiers in Fluid Dynamics*, edited by R.J. Seeger and G. Temple, Interscience, New York, 1965, Chap. 1.

[23]Jameson, A., and Caughey, D. A., "A Finite-Volume Method for Transonic Potential-Flow Calculations," *Proceedings of the AIAA 3rd Computational Fluid Dynamics Conference*, AIAA, Washington, DC, June 1977, pp. 35-54.

[24]Shmilovich, A., and Halsey, N. D., "Calculation of Transonic Flows for Novel Engine-Airframe Installations," *Proceedings of 4th Symposium on Numerical and Physical Aspects of Aerodynamic Flows*, California State Univ., Long Beach, CA, Jan. 1989.

[25]Dang, T. Q., "Calculations of Propeller/Airframe Interference Effects Using the Potential/Multienergy Flow Method," Douglas Aircraft Co., Long Beach, CA, Rept. MDC K1349, June 1988.

[26]Halsey, N. D., "Grid Generation for an Aft-Fuselage-Mounted Nacelle/Pylon Configuration," *Numerical Grid Generation in Computational Fluid Mechanics*, edited by Sengupta et al., Pineridge, 1988.

[27]Hess, J. L., and Valazero, W. O., "Calculation of Steady Flowfields Using a Surface Panel Method," Douglas Aircraft Co., Long Beach, CA, Rept. MDC J3914, Jan. 1986.